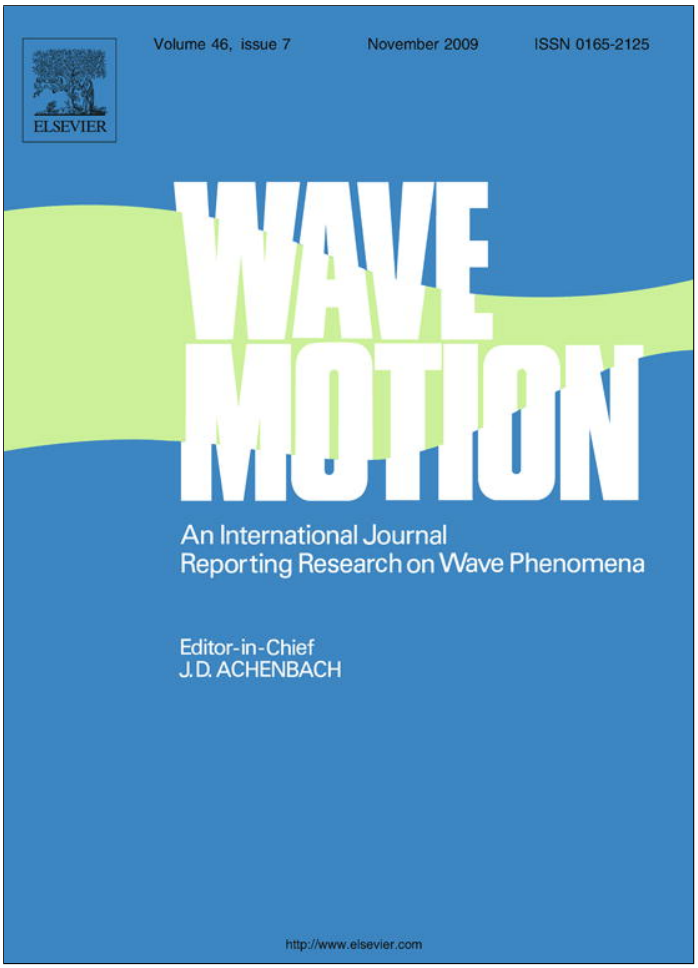

Wave Motion 46 (2009) 435–450

Contents lists available at ScienceDirect

Wave Motion

journal homepage: www.elsevier.com/locate/wavemoti

Phononic properties of hexagonal chiral lattices

Alessandro Spadoni [a], Massimo Ruzzene [a,*], Stefano Gonella [b], Fabrizio Scarpa [c]

[a] School of Aerospace Engineering, Georgia Institute of Technology, 270 Ferst Dr., Atlanta, GA, USA
[b] Department of Mechanical Engineering, Northwestern University, Evanston, IL, USA
[c] Department of Aerospace Engineering, The University of Bristol, Bristol, UK

ARTICLE INFO

Article history:
Received 24 September 2008
Received in revised form 8 April 2009
Accepted 22 April 2009
Available online 3 May 2009

Keywords:
Chiral lattices
Wave propagation
Phononic materials
Wave-guiding
Band gaps
Caustics

ABSTRACT

The manuscript reports the outcome of investigations on the phononic properties of a chiral cellular structure. The considered geometry features in-plane hexagonal symmetry, whereby circular nodes are connected through six ligaments tangent to the nodes themselves. In-plane wave propagation is analyzed through the application of Bloch theorem, which is employed to predict two-dimensional dispersion relations as well as illustrate dispersion properties unique to the considered chiral configuration. Attention is devoted to determining the influence of unit cell geometry on dispersion, band gap occurrence and wave directionality. Results suggest cellular lattices as potential building blocks for the design of meta-materials of interest for acoustic wave-guiding applications.

1. Introduction

Cellular solids, while long known and commonly exploited for disparate uses in traditional engineering applications, currently offer new opportunities to design structured materials capable of delivering unique elastic, electromagnetic, and thermal properties. The behavior of cellular materials, is strongly dependent upon their topology or spatial arrangement, providing ample opportunities in the design of novel structured configurations. Examples of unusual behavior, within the realm of solid mechanics, include auxetic or negative Poisson's ratio characteristics of re-entrant, hexagonal honeycombs, structured materials which expand perpendicularly to applied uniaxial elongation, in contrast to "classical" solids [1,2]. Periodic cellular materials are defined by the spatial repetition of an irreducible geometric domain or unit cell, and their topology, moreover, strongly affects the propagation characteristics of elastic waves. The periodicity or group of a given lattice, in fact, determines frequency bands within which the propagation of elastic waves is permitted (pass bands) or forbidden (band gaps or stop bands). Anisotropy in the elasto-dynamic behavior of periodic structural assemblies, furthermore, can be exploited to steer or guide waves in specific directions (beaming) [3,4].

Significant control afforded by structural lattices on phenomena such as band gaps and wave-beaming, owing to the large number of possible configurations and advances in manufacturing capabilities, suggest their employment as alternatives to elastic composites with periodic mass and stiffness modulations, typically known as phononic crystals. The selection of the periodic material distribution in phononic crystals, in particular, is based on the need to generate band gaps at specified frequencies, and/or to guide elastic waves along a desired path [5]. A thorough classification of unit cell classes of periodic cellular structures and associated elasto-dynamic behavior, already undertaken by [3,4] for such topologies as the hexagonal, triangular, and Kagomé lattices to name a few, may provide the possibility of designing structured materials with easily selectable wave propagation behavior.

* Corresponding author.
E-mail address: massimo.ruzzene@ae.gatech.edu (M. Ruzzene).

0165-2125/$ - see front matter © 2009 Elsevier B.V. All rights reserved.
doi:10.1016/j.wavemoti.2009.04.002

The unique characteristics of phononic materials are currently exploited in a number of applications which include sensing devices based on resonators, acoustic logic ports, wave guides and filters based on surface acoustic waves (SAW). Synthesis of phononic materials with desired band gap and wave-guiding characteristics has achieved promising maturity, mostly through the application of topology and material optimization procedures [6–8]. Although very effective, such techniques may require intensive computations and may lead to complex geometries difficult to manufacture and whose performance may lack in robustness. The application of periodic structural networks as phononic materials may potentially lead to a simplified design process, where a limited number of continuously varying parameters defines the geometry of a predefined cellular topology [9]. The successful application of this approach clearly requires identifying lattice configurations that provide sufficient design flexibility, as well as with strongly dependent elasto-dynamic properties upon a limited number of geometric parameters defining the lattice configuration.

This observation motivates the investigation of the wave propagation characteristics of the chiral structural lattice considered in this paper. The design flexibility and the unique properties of this cellular configuration, originally proposed by [10,11], and documented in a number of recent papers by the authors [12,13], are here evaluated in terms of wave propagation characteristics with the intent of broadening the already promising features offered by more traditional configurations such as triangular and hexagonal lattices proposed by [3,4]. The influence of the unit cell configuration on band gaps and wave-guiding properties is investigated through a numerical model constructed considering chiral cellular topologies as assemblies of beams connected to form a frame structure. Specifically, a compact description of the dynamic behavior of the chiral assembly is provided by an elasto-dynamic discretization based on Timoshenko beam elements [14]. Finally Bloch Theorem is employed to obtain dispersion surfaces, band diagrams, and to investigate the dependency of group speeds and phase velocities on frequency and direction of wave propagation.

The present paper is organized in five sections including the introduction above. Section 2 describes the considered lattice configuration and its geometric properties, while Section 3 describes the approach used for the analysis of free wave propagation in the lattice. Section 4 presents results in terms of dispersion surfaces, band diagrams and wave velocities and discusses their sensitivity with respect to a set of characteristic parameters for the lattice. Finally, Section 5 summarizes the objectives of the work and its main results.

2. Geometry of a hexagonal chiral lattice

2.1. Geometric parameters and properties

The structural layout of a hexagonal chiral lattice, shown in Fig. 1, consists of circular elements of radius r, acting as nodes, connected by ribs or ligaments, of length L tangent to the nodes themselves. The distance between node centers is denoted as R, while the angle between the imaginary line connecting the node centers and the ribs is defined as β. The angle between adjacent ligaments is denoted as 2θ. Finally, the wall thickness of nodes and ribs is denoted as t_c and t_b, respectively. As described in [10], the following geometric relationships hold:

$$\sin\beta = \frac{2r}{R}, \quad \tan\beta = \frac{2r}{L}, \quad \sin\theta = \frac{R/2}{R}, \quad \cos\beta = \frac{L}{R}. \tag{1}$$

The ratio L/R yields significantly different configurations, as depicted in Fig. 2, and thus is here denoted as the *topology parameter*. The unit cell of the honeycomb depicted in Fig. 2[1] is highlighted in dashed red lines, and it constitutes the smallest structural domain that encompasses the complete set of geometric entities necessary to analyze the lattice's mechanical behavior. Notably, the possible configurations obtained for variations of the topology parameter span those composed of packed circles ($L/R \to 0$) to triangular assemblies ($L/R \to 1$ or $L/r \to \infty$).

An additional geometric property of the hexagonal chiral lattice, as its name indicates, is in-plane hexagonal symmetry. As demonstrated by the third of Eq. (1), the angle θ is always 30°, indicating that the hexagonal chiral topology is invariant to in-plane rotations by the angle 2θ, regardless of the topology parameter. The influence of hexagonal symmetry on the elastostatic behavior results in a mechanical condition of in-plane isotropy [15]. The Young's modulus of a hexagonal material, as a result, is independent of direction in the plane normal to the hexagonal symmetry axis [16]. The chiral lattice, furthermore, features a negative in-plane Poisson's ratio of the order of ≈ -1 [10], and design flexibility resulting from the considerable sensitivity of mechanical behavior to the unit cell parameters L, R, θ, t_b, and t_c. For example, the static compliance of the assembly can be significantly modified by varying the topology parameter [12,13].

2.2. Unit cell configuration and lattice vectors

The structural lattice under investigation is obtained from the assembly of unit cells of the kind shown in Fig. 3. As in any periodic assembly, the location of a generic point can be described in terms of location within a reference unit cell and a set of lattice vectors which define the periodicity of the system. Introducing a reference frame in the plane of the lattice $\mathscr{F}_{\mathscr{I}}$ defined by an orthogonal unit vector basis $\mathscr{I} = (\boldsymbol{i}_1, \boldsymbol{i}_2)$, the location of a point P in cell n_1, n_2 can be expressed as:

$$\boldsymbol{\rho}_P(n_1, n_2) = \boldsymbol{r}_P + n_1\boldsymbol{e}_1 + n_2\boldsymbol{e}_2, \tag{2}$$

[1] For interpretation of color in Fig. 2, the reader is referred to the web version of this article.

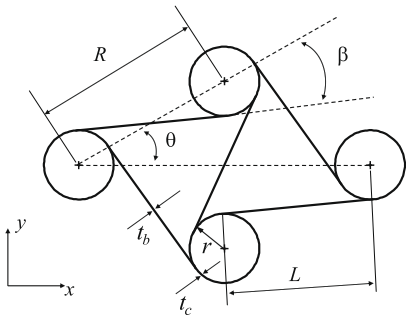

Fig. 1. Geometry of a hexagonal, chiral lattice.

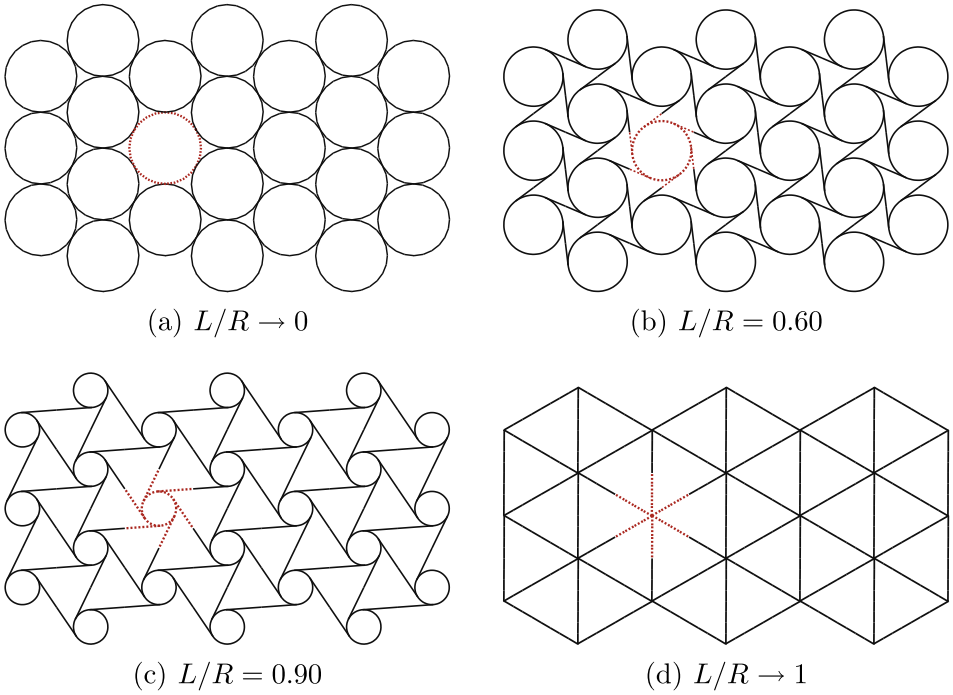

Fig. 2. Chiral configurations corresponding to increasing topology parameter L/R.

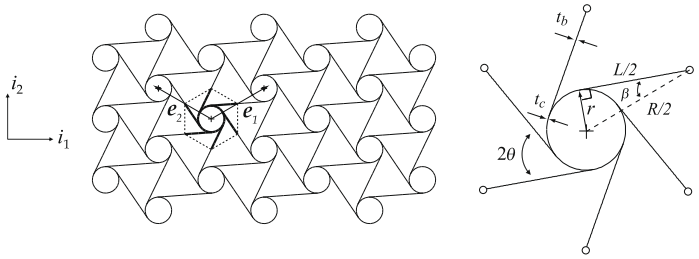

Fig. 3. Chiral structure, lattice vectors, and unit cell parameters.

where $\boldsymbol{r}_P$ defines the position of the point corresponding to P in the reference cell (0,0), while $\boldsymbol{e}_1$ and $\boldsymbol{e}_2$ are lattice vectors. The following convention of mathematical quantities is used: vectors are denoted as bold, lower case letters, capital bold letters identify matrices, and the notation $()^{\mathscr{A}}$ indicates components with respect to the vector basis $\mathscr{A}$. Accordingly, the lattice vectors for the chiral lattice can be expressed as

$$\begin{aligned} \boldsymbol{e}_1^{\mathscr{I}} &= \{R\cos\theta, R\sin\theta\}^T, \\ \boldsymbol{e}_2^{\mathscr{I}} &= \{-R\cos\theta, R\sin\theta\}^T. \end{aligned} \tag{3}$$

3. Analysis of free wave propagation

3.1. Bloch theorem

The characteristics of elastic wave propagation in periodic structural lattices can be determined by employing Bloch theorem [17]. The displacement $\boldsymbol{w}$ of a point P of the reference unit cell corresponding to a wave propagating at frequency ω can be expressed as:

$$\boldsymbol{w}(\boldsymbol{r}_P) = \boldsymbol{w}_{P_0} e^{i(\omega t - \boldsymbol{k}\cdot\boldsymbol{r}_P)}, \tag{4}$$

where $\boldsymbol{w}_{P_0}$ is the wave amplitude, $\boldsymbol{k}$ is the wave vector, and $i = \sqrt{-1}$. According to Bloch theorem, the displacement of the point corresponding to P at location $\rho_p(n_1, n_2)$ can be written in terms of the displacement of the reference unit cell as follows:

$$\begin{aligned} \boldsymbol{w}(\boldsymbol{\rho}_P) &= \boldsymbol{w}(\boldsymbol{r}_P) e^{i\boldsymbol{k}\cdot(\boldsymbol{\rho}_P - \boldsymbol{r}_P)}, \\ &= \boldsymbol{w}(\boldsymbol{r}_P) e^{i(n_1 k_1 + n_2 k_2)} \end{aligned} \tag{5}$$

where $k_i = \boldsymbol{k}\cdot\boldsymbol{e}_i$ with $i = 1, 2$. Bloch theorem, as described by Eq. (5), states that the proportionate change in wave amplitude occurring from cell to cell does not depend on the cell location within the periodic system. The wave propagation characteristics of the periodic assembly thus can be fully identified through the analysis of the reference unit cell. In the most general case of wave propagation, the wavenumber k is a complex quantity, where the imaginary part defines the amplitude attenuation (attenuation constant) as a wave propagates from one cell to the next, and a real part that defines the change of phase across each cell, and it is often called phase constant. In the analysis of wave propagation within multidimensional periodic systems, it is customary to neglect the attenuation constant, and evaluate wave motion in terms of the relation between the phase constants and frequency ω, which is expressed as a linear eigenvalue problem, as explained in the following sections. Wherever the relation between phase constants and ω is not defined, one obtains frequency gaps or stop bands, which are regions characterized by real wavenumbers indicating attenuation. For the remainder of the manuscript, the analysis of wave motion within the chiral lattice will follow the same procedure as for multidimensional periodic systems [18], whereby the terms wavenumber and wave vector will indicate quantities composed of the propagation constant only, and thus k_i will indicate a real quantity.

3.2. Reciprocal lattice and first Brillouin zone

Given the direct lattice space defined by the lattice vector basis $\mathscr{E} = (\boldsymbol{e}_1, \boldsymbol{e}_2)$, one may define a reciprocal lattice, which is described by the basis $\mathscr{B} = (\boldsymbol{b}_1, \boldsymbol{b}_2)$, whose basis vectors are given by:

$$\boldsymbol{b}_i \cdot \boldsymbol{e}_j = \delta_{ij}, \tag{6}$$

where δ_{ij} is the Kronecker delta. The reciprocal lattice vectors for the considered periodic chiral assembly are given by:

$$\begin{aligned} \boldsymbol{b}_1^{\mathscr{I}} &= \left(\frac{1}{2R\cos\theta}, \frac{1}{2(R\sin\theta)} \right)^T, \\ \boldsymbol{b}_2^{\mathscr{I}} &= \left(-\frac{1}{2R\cos\theta}, \frac{1}{2(R\sin\theta)} \right)^T. \end{aligned} \tag{7}$$

In the reciprocal lattice, the wave vector $\boldsymbol{k} = 2\pi\boldsymbol{\lambda}$ can be expressed as:

$$\boldsymbol{k} = k_1 \boldsymbol{b}_1 + k_2 \boldsymbol{b}_2, \tag{8}$$

so that, according to the definition of reciprocal lattice given in Eq. (6):

$$\boldsymbol{k}\cdot\boldsymbol{e}_1 = k_1. \tag{9}$$

While the direct lattice defines the spatial periodicity of the considered domain, the reciprocal lattice describes the periodicity of the frequency–wavenumber relation. This can be easily demonstrated by replacing $\boldsymbol{p}$, where $\boldsymbol{k} = 2\pi\boldsymbol{p}$, with $\boldsymbol{p}' = \boldsymbol{p} + m_1\boldsymbol{b}_1 + m_2\boldsymbol{b}_2$ in Eq. (5), with m_1, m_2 integers to obtain:

$$\boldsymbol{w}(\boldsymbol{\rho}_p) = \boldsymbol{w}(\boldsymbol{r}_p) e^{i(n_1 k_1' + n_2 k_2')}, \tag{10}$$

where

$$k_i' = 2\pi\boldsymbol{p}'\cdot\boldsymbol{e}_i = k_i + 2\pi m_i, \quad i = 1, 2. \tag{11}$$

Eq. (11) indicates that the wavenumber in a 2D lattice is a periodic function of the wave vector $\boldsymbol{k}$ in the reciprocal lattice. Hence, full representation of the dependency of the wave vector upon frequency is obtained by investigating its variation over a single period. In a 2D lattice, the period corresponds to a region in the reciprocal lattice whose area equals the area of the reciprocal lattice's unit cell, known as *first Brillouin zone*. Given the reciprocal lattice vectors, the first Brillouin zone is

obtained by selecting any point in the reciprocal lattice as the origin and by connecting it to all neighboring points. The perpendicular bisectors constructed on the connecting lines, also known as *Braggs lines*, define the first Brillouin zone [17]. Fig. 4a shows the reciprocal lattice vectors and the first Brillouin zone in the cartesian frame. Any symmetry in the first Brillouin zone can be utilized to identify a subregion, known as *irreducible Brillouin zone*, which is the smallest frequency–wavenumber space necessary to determine wave dispersion for a given lattice. The irreducible Brillouin zone for the chiral lattice is also highlighted in Fig. 4a, while the coordinates of the points OAB defining its boundaries are listed in Table 1.

3.3. Discretized equation of motion for the unit cell

The behavior of the unit cell can be conveniently described through a discretized equation of motion in matrix form, and by defining the cell's interaction with its neighbors (Fig. 4b). The unit cell depicted in Fig. 3 is modeled via finite-element discretization whereby components of the unit cell are treated as rigidly connected beams featuring axial, transverse, and rotational degrees of freedom (DOFs), whose behavior is governed by Timoshenko beam theory [14]. Application of standard finite-element procedures [14] yields the unit cell's equations of motion, which can be expressed as:

$$(\boldsymbol{K} - \omega^2 \boldsymbol{M})\boldsymbol{u} = \boldsymbol{f}, \tag{12}$$

where ω is the frequency of wave propagation, $\boldsymbol{K}$ and $\boldsymbol{M}$ are the global mass and stiffness matrices of the cell, while $\boldsymbol{u}$,$\boldsymbol{f}$ are, respectively, the vectors containing generalized nodal displacements and forces of interaction of the cell with its neighbors, defined as:

$$\begin{aligned} \boldsymbol{u} &= \{\boldsymbol{u}_0\ \boldsymbol{u}_1\ \boldsymbol{u}_2\ \boldsymbol{u}_3\ \boldsymbol{u}_4\ \boldsymbol{u}_5\ \boldsymbol{u}_i\}^T, \\ \boldsymbol{f} &= \{\boldsymbol{f}_0\, \boldsymbol{f}_1\, \boldsymbol{f}_2\, \boldsymbol{f}_3\, \boldsymbol{f}_4\, \boldsymbol{f}_5\ \boldsymbol{0}\}^T. \end{aligned} \tag{13}$$

In Eq. (13) the subscripts $0, 1, \ldots, 5$ follow the notation described in Fig. 4b, while subscript i denotes the degrees of freedom of internal cell nodes. Fig. 4b also shows the considered unit cell discretization, highlights the internal nodes (white circles), and lists boundary nodes and forces (dark squares). The considered cell discretization approximates the circles as a sequence of straight beams, avoiding the complexity associated with a finite-element discretization of curved elements [19], and has been chosen based on convergence studies performed on the dispersion relations in the frequency range considered relevant for the analysis presented in what follows. A detailed description of this convergence study is here omitted for the sake of brevity. The proposed discretization, moreover, captures up to 198 wave modes, while the current analysis only considers wave modes up to the 20th thus avoiding numerical error at high-frequencies due to spatial sampling. Finally, Eq. (13) relies on the assumption that no external forces are applied, and that only the interaction forces with neighboring cells appear in the cell's equation of motion.

3.4. Evaluation of dispersion relations

According to Bloch theorem, periodic boundary conditions relate the cell's generalized displacements, and equilibrium conditions are enforced to the generalized forces applied to consecutive cells:

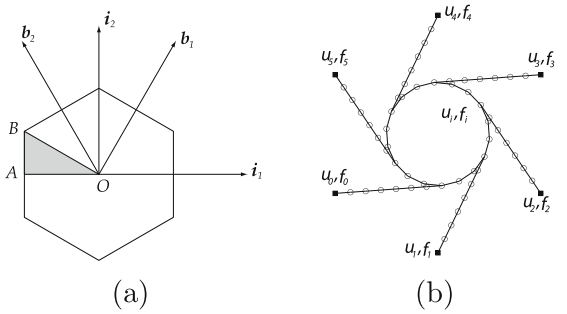

Fig. 4. First and irreducible Brillouin zones and lattice vectors in cartesian space (a); (b) unit cell discretization and detail of internal and boundary degrees of freedom and interaction forces.

Table 1
Coordinates of corner points of the irreducible Brillouin Zone for chiral lattices.

	Cartesian frame	Reciprocal lattice frame
O	(0, 0)	(0, 0)
A	$\left(\frac{-1}{2R\cos\theta}, 0\right)$	$\left(-\frac{1}{2}, \frac{1}{2}\right)$
B	$\left(\frac{-1}{R\cos\theta}, \frac{1}{6R\sin\theta}\right)$	$\left(-\frac{1}{3}, \frac{2}{3}\right)$

$$\begin{aligned} \boldsymbol{u}_3 &= e^{ik_1}\boldsymbol{u}_0, \\ \boldsymbol{u}_4 &= e^{i(k_1+k_2)}\boldsymbol{u}_1, \\ \boldsymbol{u}_5 &= e^{ik_2}\boldsymbol{u}_2, \end{aligned} \tag{14}$$

and

$$\begin{aligned} \boldsymbol{f}_3 &= -e^{ik_1}\boldsymbol{f}_0, \\ \boldsymbol{f}_4 &= -e^{i(k_1+k_2)}\boldsymbol{f}_1, \\ \boldsymbol{f}_5 &= -e^{ik_2}\boldsymbol{f}_2. \end{aligned} \tag{15}$$

Eqs. (14) and (15) can be rewritten in matrix form as follows:

$$\boldsymbol{u} = \boldsymbol{T}_u \boldsymbol{u}_r, \tag{16}$$

$$\boldsymbol{f} = \boldsymbol{T}_f \boldsymbol{f}_r, \tag{17}$$

where $\boldsymbol{u}_r = \{\boldsymbol{u}_0\ \boldsymbol{u}_1\ \boldsymbol{u}_2\ \boldsymbol{u}_i\}^T$, and $\boldsymbol{T}_f = \boldsymbol{T}_u^T$. Substituting Eq. (14) into Eq. (12), and pre-multiplying the resulting equations by T_u^H, with $()^H$ denoting a complex conjugate transpose, yields:

$$[\boldsymbol{K}_r(k_1,k_2) - \omega^2 \boldsymbol{M}_r(k_1,k_2)]\boldsymbol{u}_r = \boldsymbol{0}, \tag{18}$$

where $\boldsymbol{K}_r(k_1,k_2)$, $\boldsymbol{M}_r(k_1,k_2)$ are reduced stiffness and mass matrices. Eq. (18) constitutes an eigenvalue problem whose solution defines the dispersion characteristics of the lattice. Its solution requires imposing two of the three unknowns k_1, k_2, ω, and solving for the third. In the current approach, wavenumbers k_1, k_2 vary within the first Brillouin zone. The solution of Eq. (18) yields the frequency of wave propagation, corresponding to the assigned pair k_1, k_2. Solutions obtained for k_1, k_2 spanning the entire first Brillouin zone define the dispersion surfaces of the lattice, here denoted as $\omega = \omega(k_1, k_2)$. The number of surfaces obtained corresponds to the dimensions of the eigenvalue problem in Eq. (18), which in turn, is defined by the number of reduced DOF's $\boldsymbol{u}_r$. Each surface describes the wavenumber–frequency relation for the corresponding wave mode.

3.5. Phase speeds and group velocities

Dispersion surfaces allow the evaluation of phase and group velocities and their dependency on frequency and direction of propagation. The wave vectors in the reciprocal and geometric space are, respectively, expressed as:

$$\boldsymbol{k} = k_1\boldsymbol{b}_1 + k_2\boldsymbol{b}_2 = \xi_1\boldsymbol{i}_1 + \xi_2\boldsymbol{i}_2.$$

The phase velocity at a given frequency ω is given by:

$$\boldsymbol{c}_{ph} = \frac{\omega}{k}\boldsymbol{u}, \tag{19}$$

where $k = |\boldsymbol{k}|$ and $\boldsymbol{u}$ is a unit vector in the direction of the wave vector ($\boldsymbol{u} = \boldsymbol{k}/k$). The information provided by the phase velocity is essentially the same as that obtained from constant-frequency contours of the dispersion surfaces. In fact, for non-dispersive media, the two representations can be combined in the form of *slowness curves* [18]. In the case of periodic lattices, useful information is provided by direct representation of the phase speed. Such description elucidates the increasingly dispersive and orthotropic nature of wave propagation as frequency ω increases. The phase speed c_{ph} is evaluated by selecting iso-frequency contours from dispersion surfaces at a desired frequency value. The angular range spanned by the corresponding set of wavenumbers is then computed to obtain the angular variation of the phase speed in terms of direction. For a general non-dispersive, isotropic medium, this operation yields a circle whose radius is independent of frequency.

Important indications regarding the energy flow associated with the propagation of wave packets within the lattice are provided by the group velocity, which can be evaluated as follows:

$$\boldsymbol{c}_g^{\mathcal{F}} = \left(\frac{\partial\omega}{\partial\xi_1}, \frac{\partial\omega}{\partial\xi_2}\right)^T. \tag{20}$$

The group velocity defines the direction of energy flow within the structure, and can be used to identify preferential or forbidden directions of wave propagation [3]. Such forbidden propagation zones are the result of interference phenomena resulting from the propagation of waves at the same frequency and different wave vector directions, and can be observed over a broad range of frequencies in anisotropic materials and structures [20]. Results presented in the following sections will show how dispersion and anisotropy in chiral lattices strongly influence the characteristics of wave propagation particularly as frequency increases.

4. Results

Results reported in the current and following sections consider a lattice made of aluminum (Young's modulus $E = 71$ GPa, Poisson's ratio $v = 0.33$, and density $\rho = 2700$ Kg/m^3) composed of a frame of beam-like components with rectangular

cross- section. A reference configuration defined by the geometric dimensions listed in Table 2 is first employed to present salient characteristics of wave propagation in a chiral lattice. The same reference configuration is also employed in subsequent parametric studies to highlight the influence of geometric arrangement on wave propagation characteristics of chiral lattices. Results are presented in terms of the non-dimensional frequency Ω:

$$\Omega = \frac{\omega}{\omega_0}, \tag{21}$$

where:

$$\omega_0 = \pi^2 \sqrt{\frac{E t_b^2}{12 \rho L^4}}, \tag{22}$$

corresponds to the first flexural frequency of a ligament of length L assumed in a simply supported configuration. Although simple supports do not reproduce the actual boundary conditions on the ligaments, the expression of ω_0 has been selected as a reference measure of frequencies at which the internal members of the lattice undergo resonance, and for which the dynamic deformations of the lattice are dominated by local behavior.

4.1. Dispersion surfaces

Fig. 5 presents contours of dispersion surfaces corresponding to the first four wave modes of the lattice defined by the dimensions in Table 2. The first Brillouin zone, represented in Fig. 5 is superimposed to the iso-frequency contours to highlight the correctly captured periodicity of the frequency–wavenumber spectrum. Furthermore, the irreducible Brillouin zone, depicted in Fig. 5 as a shaded gray area, effectively describes all the characteristics of dispersion by taking advantage of the symmetry present in the the first Brillouin zone.

The hexagonal symmetry of the chiral lattice clearly transpires in the elasto-dynamic response represented in Fig. 5, where six-lobed contour curves denote the dispersion relations of all considered wave modes, a feature that becomes more apparent as frequency increases. A very interesting attribute of the first two wave modes, moreover, is provided by the "leveling-off" of the dispersion surfaces which appear to change rapidly at low frequencies, and become virtually flat as frequency increases. This behavior is indicated by the presence of a large number of iso-frequency contour lines at low wavenumbers, and by their much lower density towards the edges of the first Brillouin zone (see Fig. 5a and b). The opposite happens for the third and fourth modes, which are characterized by rapid changes at high wavenumbers and almost flat surfaces around $k_1, k_2 \approx 0$ (see Fig. 5c and d). This implies that the wave speeds associated with wave modes 3 and 4 change significantly within the first Brillouin zone. Finally, of note is the fact that circular iso-frequency contour curves associated with low frequency and wave number depicted in suggest isotropic elasto-dynamic behavior of the chiral lattice, specifically for the first and second wave modes.

4.2. Band diagrams

A convenient representation of the dispersion characteristics is provided in the form of band diagrams, whereby the frequency of wave propagation is plotted against the magnitude of the wave vector as it varies along the contours of the irreducible Brillouin zone. This is done to obtain maxima and minima of each wave mode in order to establish the presence of band gaps [17]. Wave propagation behavior within the irreducible Brillouin Zone has already been addressed in Fig. 5. Fig. 6 compares the band diagram for the reference lattice specified in Table 2 with that of a lattice defined by a topology parameter $L/R = 0.60$ (see Fig. 2). The remaining parameters are retained as for Table 2. In order to maintain the ligament length L unchanged, variations in the topology parameter are made to coincide with variations in the distance between the node centers R, and node radius r.

The band diagram associated with topology parameter $L/R = 0.90$ (Fig. 6a) highlights very interesting characteristics, some of which confirm the conclusions made from the analysis of the dispersion surfaces. Namely, the curve corresponding to the third mode appears almost flat, which implies that wave packets of this particular polarization propagate very slowly within the lattice, and may have a behavior which is closer to that of standing waves over most of the wavenumber

Table 2
Reference lattice dimensions.

Parameter	Value
Ligament length	$L = 26.4$ mm
Ligament wall thickness	$t_b = 0.5$ mm
Node radius	$r = 6.4$ mm
Node wall thickness	$t_c = 0.5$ mm
Slenderness ratio	$t_b/L = 1/52$
Topology parameter	$L/R = 0.90$

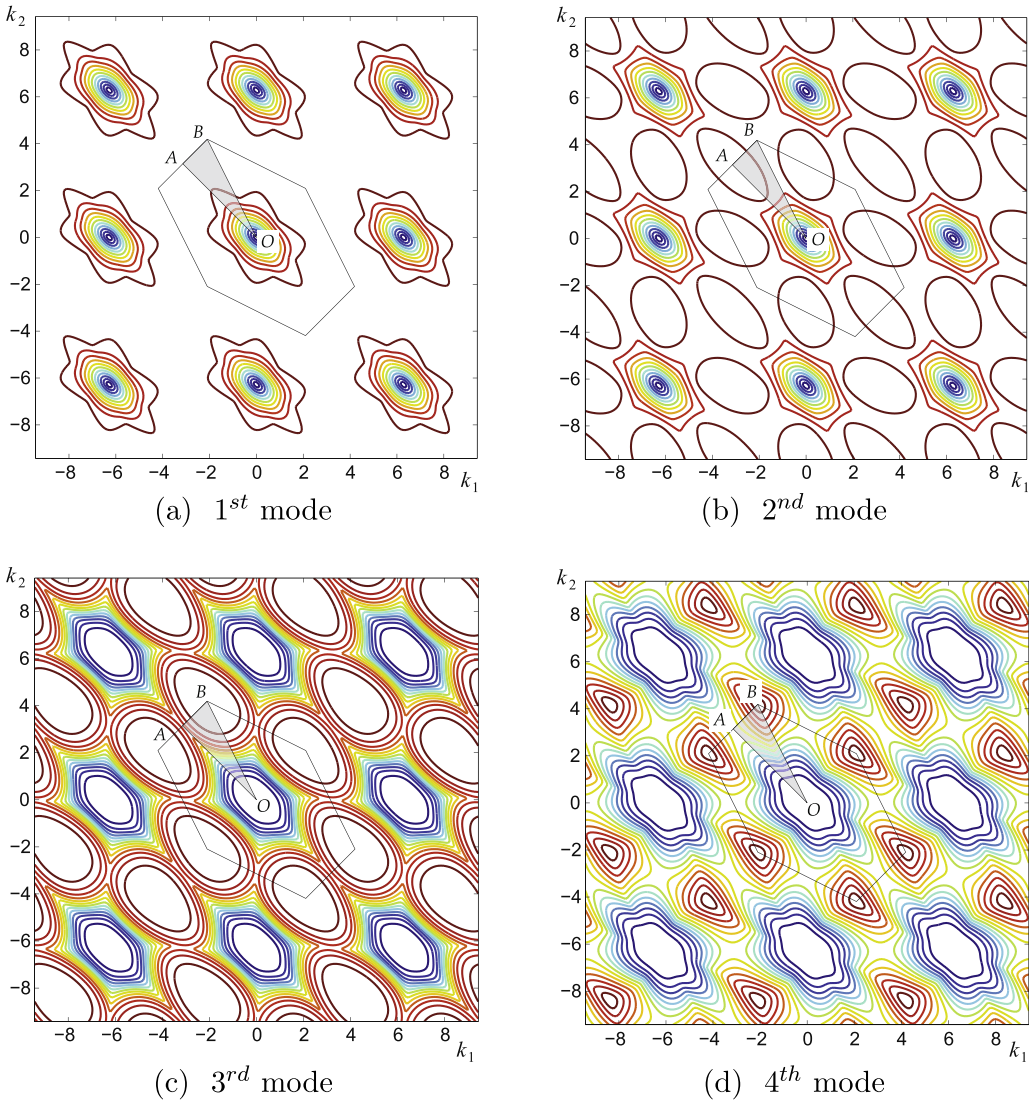

Fig. 5. Iso-frequency contours of the dispersion surfaces and detail of first and irreducible Brillouin zones.

spectrum. The two lowest modes, typically associated to *P* (longitudinal) and *S*-polarized (transverse) modes in solid materials, are approximately non-dispersive up to $\Omega \approx 1$. This is common in most cellular structures, and it is often used as the basis for the quasi-static approximation of their equivalent mechanical properties [4,21]. In [4], for example, it is shown how the equivalent shear and bulk moduli for hexagonal and triangular lattices can be obtained through the following relations:

$$c_P = \sqrt{\frac{G^* + K^*}{\rho^*}}, \quad c_S = \sqrt{\frac{G^*}{\rho^*}}, \tag{23}$$

where c_P, c_S, respectively, denote the long wavelength approximations of the phase speeds of *P* and *S* waves, while G^*, K^*, ρ^* are the equivalent shear, bulk moduli, and density of the lattice. These relations are based on the expressions of the phase speeds of an isotropic elastic medium in- plane stress. In Fig. 6a, the first two modes within the non-dispersive range appear practically overlapped, which indicates that the two modes propagate virtually at the same phase speeds, i.e. $c_P \approx c_S$. The assumption that in the low frequency range the chiral lattice behaves according to the laws of two-dimensional elasticity for an isotropic medium would lead to the conclusion that $G^* \gg K^*$, which would seem to confirm the results from previous investigations predicting an in-plane Poisson's ratio $\nu \approx -1$ [10]. It is however important to underline that, due to the lattice topology producing non-central forces [22] as well as rotation of the nodes or circles, the two-dimensional equations of elasticity for isotropic materials in plane stress may not accurately describe the equivalent behavior of the lattice, even at long wavelengths. The consideration of higher order elasticity models, such as micropolar continuum theories, may be needed in order to capture nodal rotations and their effect on the mechanical properties of the structure [22]. Homogenized mechanical properties for chiral lattice configurations similar to the one analyzed in the current work have been analyzed in [23] using flexural–hinging–stretching models based on the approach formulated by Masters and Evans [24]. Chiral lattices considered

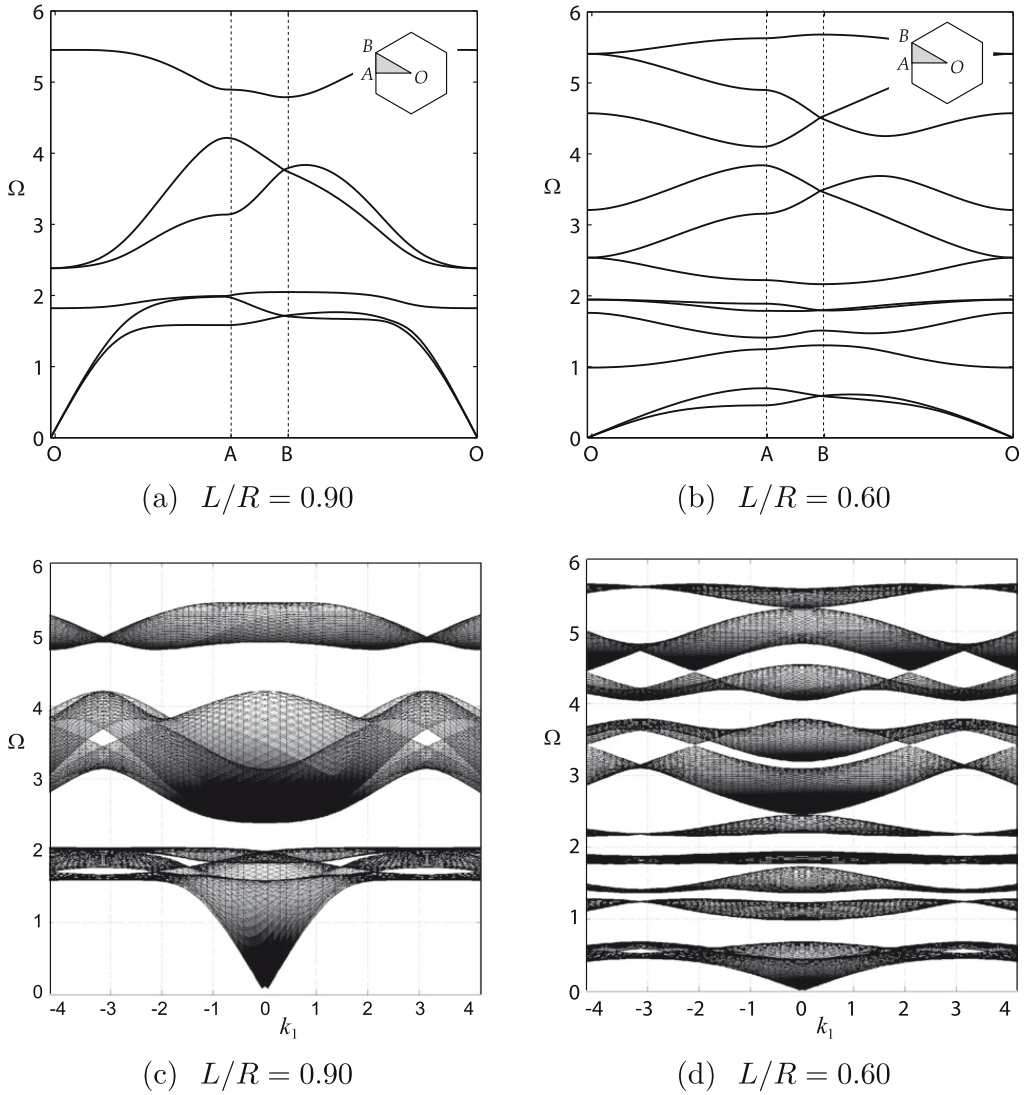

Fig. 6. Band diagrams for $L/R = 0.90$ (a) and $L/R = 0.60$ (b) lattices with associated dispersion surfaces (c) and (d).

by Grima et al. [23] present a transversely isotropic, static behavior, confirming that structural chirality has no effect on the static, mechanical properties of a material [22]. In-plane orthotropic, elasto-static properties, however, also characterize chiral tessellations of order n, where n denotes the number of ligaments connecting nodes or circles [23]. In contrast to analytical analyses appeared in the literature so far [10,23], the current FE model features nodes or circles with in-plane flexural and axial deformation behavior capturing anisotropic elasto-static/dynamic behavior related to the first-order moduli of elasticity [25]. The identification of equivalent mechanical properties for the lattice through the asymptotic analysis of the dispersion relations goes beyond the scope of the present work and is the subject of current investigations.

An additional feature of the chiral lattice defined by $L/R = 0.90$ transpiring from the band diagram of Fig. 6a and the associated dispersion surfaces of Fig. 6c is the presence of two large band gaps, centered approximately at $\Omega = 2.1$ and $\Omega = 4.5$, which suggests the considered lattice configuration as a superior phononic meta-material than what would be possible by employing other known geometries. Among the configurations investigated by Phani et al. [4], in fact, the triangular lattice was the only arrangement to feature a band gap at low frequencies. The chiral lattice, hence, appears as a superior candidate at least for applications requiring stop band capabilities, in that it features low frequency band gaps of considerable extent. A comparison of the chiral and triangular lattices (the latter obtained by letting $L/R \to 1$) is provided by the parametric studies presented in the following sections.

Fig. 6b shows the band diagram of a lattice characterized by a ratio $L/R = 0.60$. The changes in modal structure, modal density and band gap location are very evident, demonstrating how a single configurational parameter strongly affects the dispersion characteristics of the lattice. The $L/R = 0.60$ lattice, in particular, is characterized by a low frequency band gap, also visible in the associated dispersion surfaces of Fig. 6d, which separates the first two branches from the third. In addition, the slope of the first two branches and the corresponding wave velocities are significantly lower than for the $L/R = 0.90$ lattice.

Both band diagrams portrayed in Fig. 6a and b present wave modes that appear to cross. For the structural lattice at hand in actuality, they approach each other and then suddenly diverge. This phenomenon is known as eigenfrequency-loci veering. It is present in systems with weakly coupled modes and may be associated with spatial and directional localization of disturbances [26,27]. This is however not always the case: other cases may feature crossing eigenvalues [28]. The repercussions of eigenfrequency-loci veering have been previously mentioned by [4,26–28], among others, and are still a topic of research. The current work is instead aimed at studying band gaps and wave directionality for a novel structural lattice.

An attempt to explain the occurrence of band gaps between different sets of dispersion branches as the geometry of the lattice varies can be undertaken through the analysis of the associated wave modes shown in Fig. 7. Fig. 7a displays the modes corresponding to the first five dispersion branches of the $L/R = 0.90$ lattice, calculated at the vertices O, A, and B of the irreducible Brillouin zone. The first and second mode at O correspond to a rigid-body mode, while the modes associated with locations A and B show how propagation for these polarizations occurs mostly through bending of the ligaments. The third mode is characterized by rotation of the circular node, while the fifth mode is the first for which relevant deformations of the circle can be observed. In particular, the mode at A corresponds to the lower bound of the second band gap which suggests how its occurrence may be related to relevant deformations of the circles within the unit cell. The fourth mode is not presented due to its lack of distinctive features and for the sake of brevity. Wave modes associated with $L/R = 0.60$ and depicted in Fig. 7b seem to confirm the notion that the generation of the lowest band gap is mostly associated with significant internal deformations of the circles. Such deformations are evident for the second mode at A, which corresponds to the lower limit of the first band gap of the $L/R = 0.60$ lattice. This behavior also suggests that the circles may behave as internal inclusions in the lattice and that their stiffness and mass may be properly selected to achieve desired band gap characteristics.

Band gap occurrence estimated via unit cell analysis is verified by computing the harmonic response of lattices of finite extent for frequencies of excitation varying within the range considered in the band diagrams of Fig. 6. The lattices comprise 13×17 chiral unit cells, and they are considered as simply supported along their edges. A in-plane harmonic load is applied at the center of the lattice. The same discretization and finite-element formulation used for the unit cell analysis are employed for the generation of the discretized model of the finite lattice. The resulting finite-element model predicts the lattice displacements at nodal locations, whose root mean square sum is computed to estimate the response characteristics of lattices of finite extent at various frequencies. The results for the two lattices ($L/R = 0.90$ and $L/R = 0.60$) clearly show the presence of band gaps, at the frequencies predicted by the unit cell analysis and demonstrate the corresponding strong filtering effects on the response of the finite lattice (Fig. 8).

4.3. Influence of unit cell geometry on band gaps

The results presented in the previous section suggest the need for an investigation of the influence of unit cell geometry on width and location of possible band gaps. Specifically, attention is devoted to the effects of node wall thickness t_c and of the topology parameter L/R. Both parameters affect the relative density of the lattice, defined as follows:

$$\frac{\rho^*}{\rho} = \frac{2\sqrt{3}}{3}\frac{(2\pi r t_c + 3L t_b)}{R^2}. \tag{24}$$

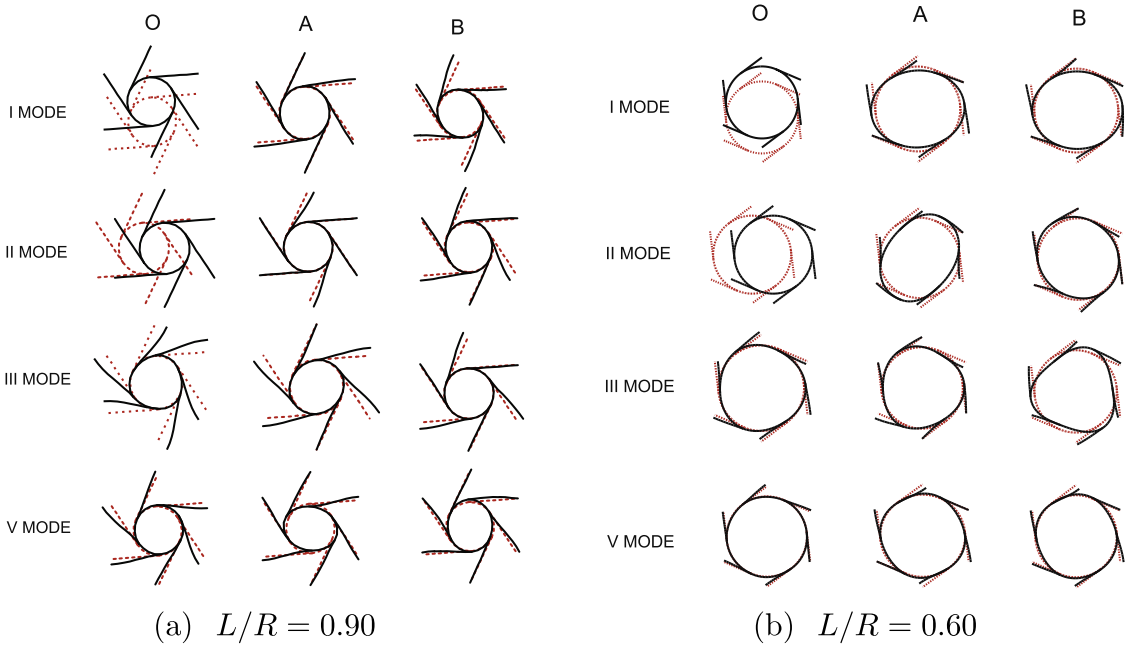

Fig. 7. First, second, third and fifth wave modes at vertices O, A, and B of the *irreducible Brillouin zone.*

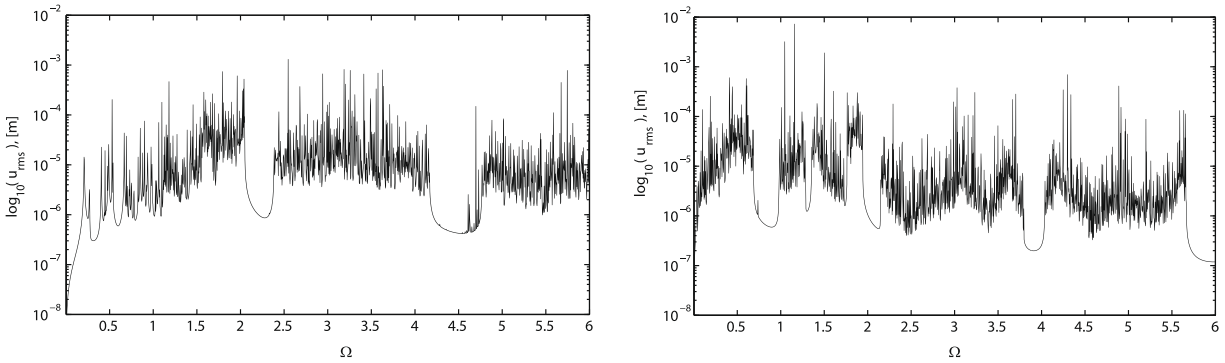

(a) $L/R = 0.90$ (b) $L/R = 0.60$

Fig. 8. Root mean square response of finite lattices subjected to harmonic loads.

The relation between stiffness and mass of the circles and of the ligaments strongly affects the location and extent of band gaps. An obvious way to specify stiffness and mass of the circles is to change their wall thickness t_c, while reducing the L/R ratio corresponding to an increase in the radius r, and in turn to a reduction in the bending stiffness.

The extent and location of band gaps, as related to circle wall thickness, is evaluated for two lattices defined by $L/R = 0.60$ and $L/R = 0.90$. The results in Fig. 9a and b, where band gaps are represented as dark regions, show large sensitivity of the elasto-dynamic behavior of chiral lattices with respect to the circles' wall thickness t_c. This indicates t_c is a crucial design parameter which can be properly selected to obtain band gaps at desired frequencies. It is interesting to observe how large band gaps at higher frequencies appear as having a center frequency which increases with t_c. This suggests that the resulting added stiffness of the nodes causes their bending deformation to occur at higher frequencies, and confirms how this is a leading mechanism for band gap occurrence (see Fig. 7). Finally, the first gap for $L/R = 0.90$ lattice appears to become independent upon t_c for $t_c/t_{c_0} > 1$, which may indicate that the increase in stiffness is counterbalanced by the corresponding increase in mass. A second study considers the dependence of band gaps upon topology parameter L/R. Results for two values of wall thickness are presented in Fig. 9c and d. Specifically, results in Fig. 9c are obtained for the minimum value of the previously considered t_c range, i.e. $t_c/t_{c_0} = 0.2$, which corresponds to extremely thin circles, while the results in Fig. 9d are associated with the reference wall thickness value $t_c/t_{c_0} = 1$. These results elucidate how the topology parameter L/R can be used as a

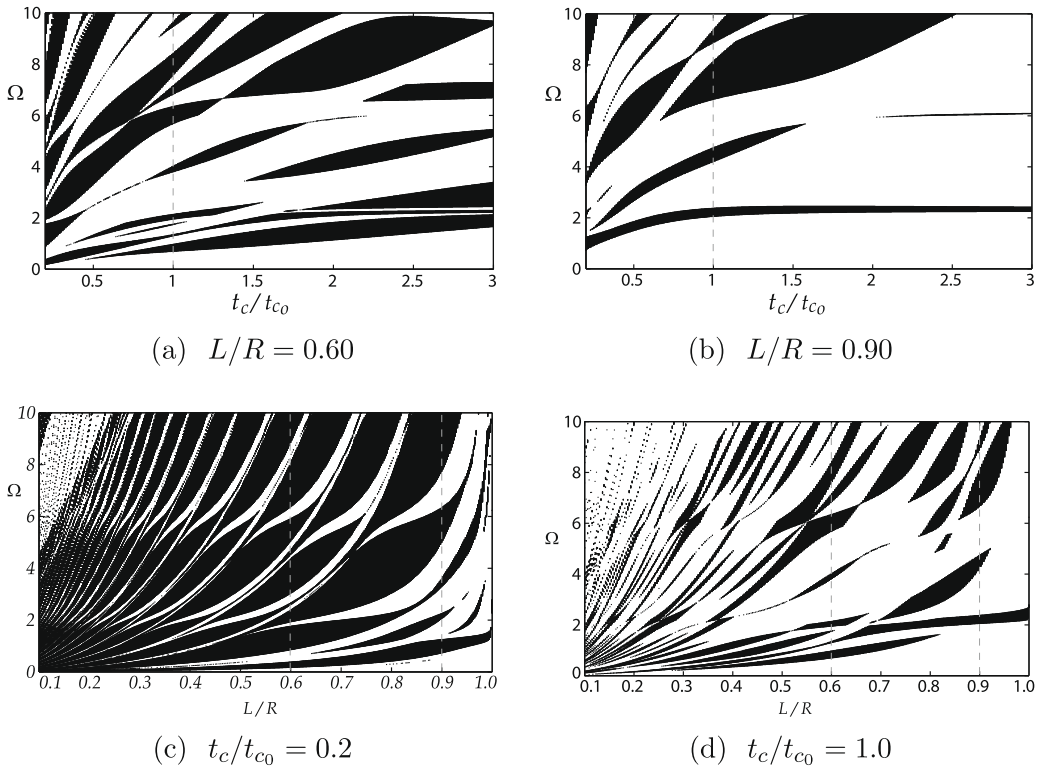

(a) $L/R = 0.60$ (b) $L/R = 0.90$

(c) $t_c/t_{c_0} = 0.2$ (d) $t_c/t_{c_0} = 1.0$

Fig. 9. Band gap dependence upon t_c/t_{c_0} (a,b) and upon L/R (c,d).

tuning parameter for band gaps. The range of variation of L/R explores all the possible topologies which vary from a packed assembly of circles (see Fig. 2) obtained for $L/R \to 0$, to the triangular lattice corresponding to $L/R \to 1$. It is interesting to note that for the latter (i.e. $L/R \to 1$), the obtained band gaps match exactly those predicted for a triangular lattice as reported in [4]. The results presented in Fig. 9 demonstrate the design flexibility of the considered periodic lattice configuration. Of the two considered parameters, the wall thickness t_c appears as the most interesting one, as it allows tuning of the band gap distribution to be performed without the need for changes in the overall topology of the assembly. From this perspective, one may envision a manufacturing procedure which is able to generate the chiral lattice, and allows the flexibility to modify the wall thickness of the circles either locally, to introduce a discontinuity in periodicity, or over a number of consecutive cells defining a path along which acoustic waves need to be guided.

4.4. Phase speeds and group velocities

A final analysis considers the dependence of phase speeds and group velocities upon frequency, direction, and lattice topology. The evaluation of wave speeds provides important indications on the anisotropic nature of the lattice within a specified frequency range, it shows the existence of preferential directions of propagation and energy flow, and defines the dispersive nature of the medium. Dispersion, directionality and anisotropy all lead to wave-interference phenomena, which can be also exploited for effective focusing of the acoustic energy associated with propagating waves [3,20]. Attention is devoted to the wave velocities of the first three modes, which could be directly associated with the wave modes of an equivalent isotropic medium, with the purpose of estimating the equivalent mechanical properties of the lattice along the lines of [4,21]. In all results, velocities are normalized with respect to the phase velocity of the first mode estimated for $k_i \to 0, \omega \to 0$, which corresponds to the long wavelength, low frequency range where group and phase speeds are expected to be approximately equal.

Results for phase velocity corresponding to the first three modes for lattices defined by topology parameter $L/R = 0.90$ are reported in Fig. 10. The polar plots, which are obtained for a lattice with all dimensions fixed to the values listed in Table 2, present the variation of phase velocity magnitude for various values of the normalized frequency. Curves for phase velocities corresponding to the first and second mode are approximately circular at low frequencies, while they highlight the lattice anisotropy as frequency increases. A general trend for the first and second mode shows a decreasing phase speed as frequency increases. This behavior is in agreement with the fact that the corresponding dispersion branches in Fig. 6b are characterized by a decreasing slope as the wave vector approaches the edges of the first Brillouin zone. It is also interesting that the third mode shows a cut-off frequency at $\Omega \approx 1$, and a very limited variation over the first Brillouin zone. The presence of a cut-off frequency and an almost flat dispersion branch correspond to a phase velocity which approximately varies hyperbolically with respect to the wavenumber. This is confirmed by the strong variation in phase velocity observed over the considered frequency range for the third mode.

Group velocity dependence upon frequency and direction for the considered configuration is presented in Fig. 10. As expected, the group velocity for the first two modes in the low frequency limit are nearly identical to the corresponding phase velocities, confirming the non-dispersive behavior for long wavelengths. As frequency increases, however, group velocities show a very complex behavior which is characterized by caustics (cusps in group velocity distributions) of the kind observed in anisotropic media [20]. Such caustics are associated with strong energy focusing for propagating wave packets, resulting from interference between the various wave components propagating in the lattice plane. The behavior of lattices with $L/R = 0.60$ shows similar trends in terms of both phase and group velocities and are here omitted for the sake of brevity.

The appearance of caustics in the group velocity diagrams of all considered wave modes and configurations is to be attributed to inflection points in the wave-front diagrams of Fig. 5. Focusing of energy along preferential directions is demonstrated by selecting the third wave mode for a lattice with $L/R = 0.90$ and the corresponding iso-frequency contour at the normalized frequency $\Omega = 1.92$ (Fig. 11a). An arbitrarily chosen set of wave vectors, numbered 1–9, corresponds to as many group velocities ($\overline{c_g}$) directions, also numbered 1–9. While the set of wave vectors approximately spans 90°, the corresponding group velocity directions, which are normal to the iso-frequency contours, appear to be mostly confined to two orientations as depicted in Fig. 11b. If a large set of wave vectors spanning 360° is considered (Fig. 11c), the corresponding group velocity vectors are mostly oriented in six directions as shown in Fig. 11d. In certain instances however, it is possible to have the direction of group velocity coincide to that of wave vectors. This may occur only if the wave vector direction coincides with a symmetry axis of the frequency/wavenumber spectrum [20]. Collinearity of wave vectors and associated group velocity directions is confirmed in Fig. 11c, where the dashed arrow describes a group velocity vector collinear to a given wave vector. The hexagonal symmetry of the chiral lattice, which also transpires in the frequency/wavenumber spectrum, then produces at least six such loci. Perfectly circular iso-frequency contours on the other hand, indicate that the direction of group velocity is always parallel to that of the wave vectors, and moreover, that the frequency/wavenumber spectrum possesses infinite axes of symmetry.

The presence of caustics in the group velocity diagrams is a feature observed in the ballistic phonon propagation in crystals and it has been attributed to elastic anisotropy of the medium [29–31]. In order to confirm preferential energy flux within the chiral lattice, a FE macro-lattice model composed of 25 cells (Fig. 1) in the x-direction and 41 macro cells in the y-direction is considered. Both ligaments and nodes are assumed to have a rectangular cross-section and the dimensions and material properties reported in Table 2 and Section 4, respectively. Ligaments are discretized by six elements, while nodes are discretized by 12 elements. Employing a Timoshenko beam-element model [14], the FE model results in 166,410 DOF's.

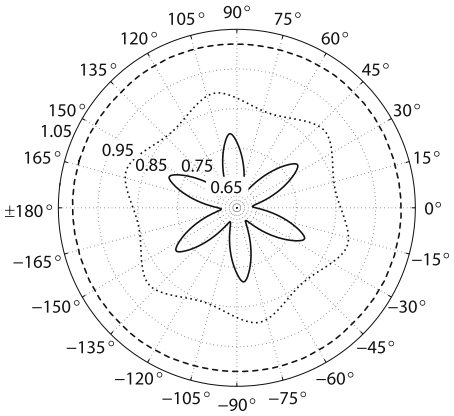

(a) Mode 1: - - - $\Omega = 0.30$, $\cdots$ $\Omega = 1.30$, — $\Omega = 1.55$

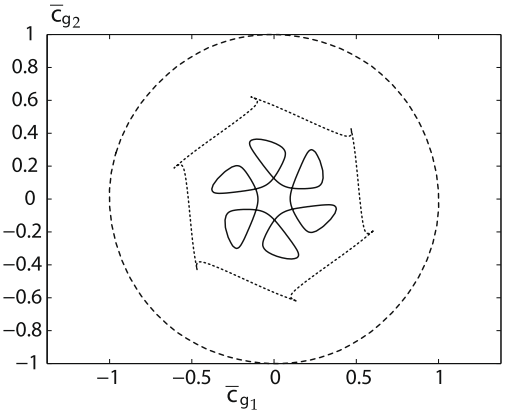

(b) Mode 1: - - - $\Omega = 0.30$, $\cdots$ $\Omega = 1.30$, — $\Omega = 1.55$

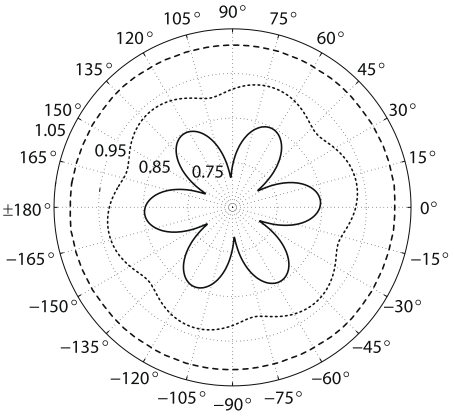

(c) Mode 2: - - - $\Omega = 0.30$, $\cdots$ $\Omega = 1.30$, — $\Omega = 1.62$

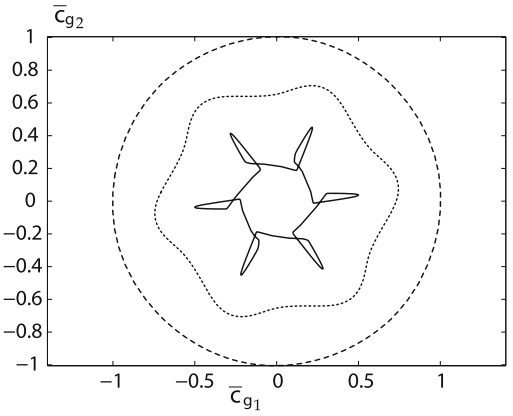

(d) Mode 2: - - - $\Omega = 0.30$, $\cdots$ $\Omega = 1.30$, — $\Omega = 1.62$

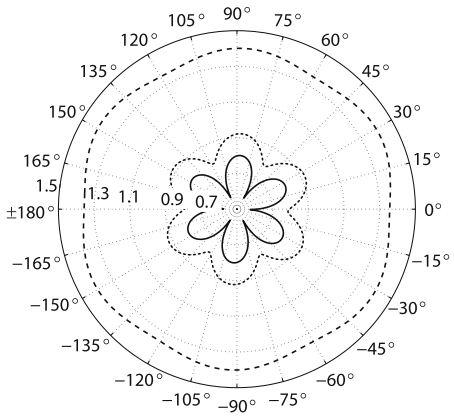

(e) Mode 3: - - - $\Omega = 1.84$, $\cdots$ $\Omega = 1.92$, — $\Omega = 1.97$

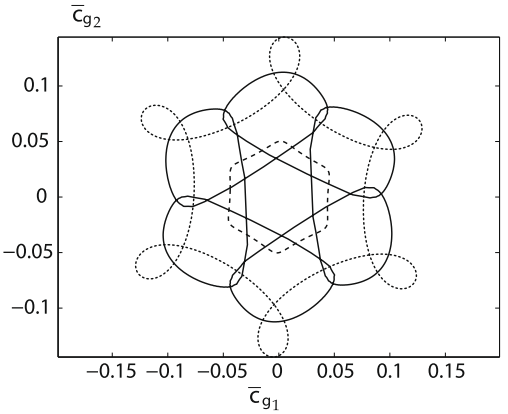

(f) Mode 3: - - - $\Omega = 1.84$, $\cdots$ $\Omega = 1.92$, — $\Omega = 1.97$

Fig. 10. Phase and group velocities versus frequency for a lattice with $L/R = 0.90$ for wavemode 1 (a,b), 2 (c,d), and 3 (e,f).

The considered input is a point load applied on the node closest to the center of the macro-lattice. Such input is intended to excite the normalized frequency $\Omega = 1.62$ in order to induce the group velocities depicted in Fig. 12a, which belong to the first and second wavemodes. The considered input is a four-cycle harmonic burst modulated by a hanning window (Fig. 12b). The induced nodal displacements and velocities are integrated in time by way of the Newmark implicit scheme with a sampling frequency of 20 intervals per wave cycle. The resulting total energy in each element $\boldsymbol{E}_e(t)$ can then be evaluated as [14]:

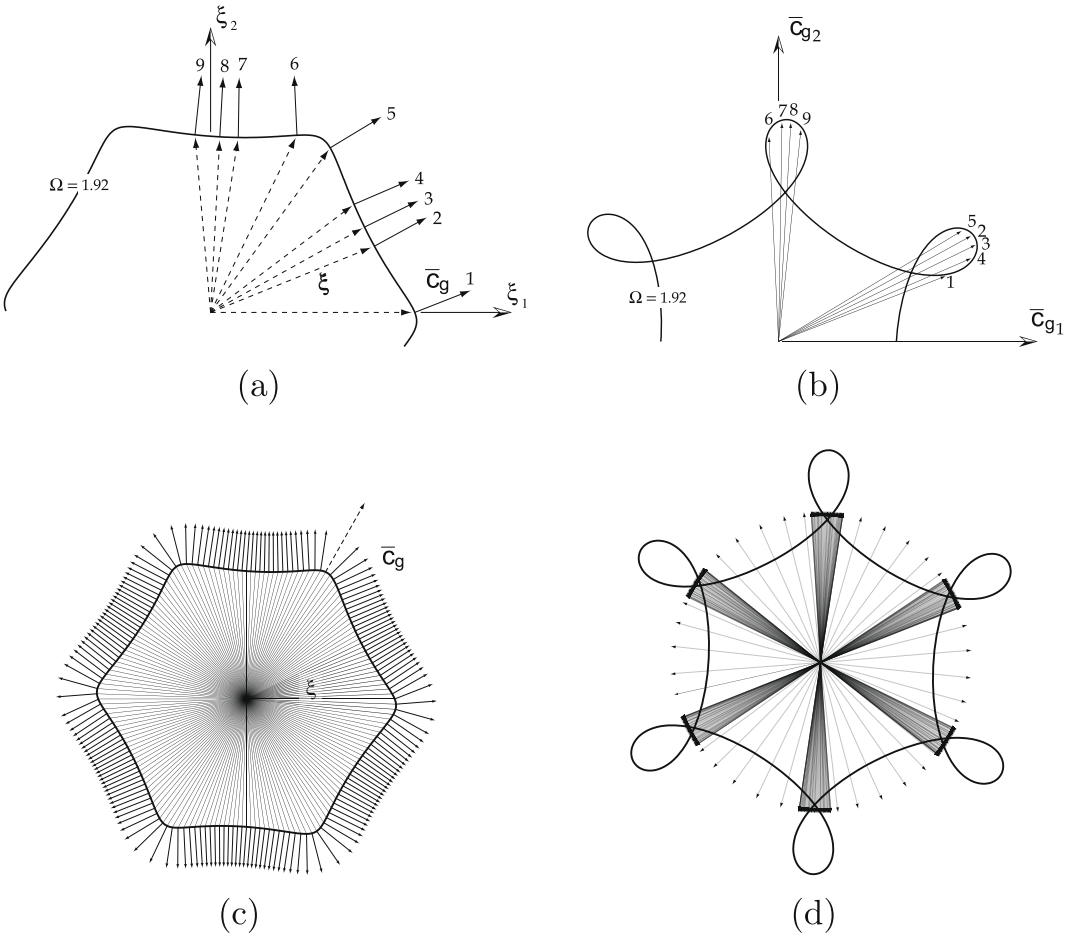

Fig. 11. Caustics stemming from group velocity for $L/R = 0.90$, wave mode 3 and $\Omega = 1.92$.

$$\boldsymbol{E}_e(t) = \frac{1}{2}\boldsymbol{u}_e^T \boldsymbol{K}\boldsymbol{u}_e + \frac{1}{2}\dot{\boldsymbol{u}}_e^T \boldsymbol{M}\dot{\boldsymbol{u}}_e, \tag{25}$$

where $\boldsymbol{u}_e$ and $\dot{\boldsymbol{u}}_e$ are the nodal displacements and velocities belonging to each element e. The energy of is quantified as the average total energy per wave period as follows:

$$\overline{\boldsymbol{E}}_e = \frac{1}{T}\int_{t_i}^{t_i+T} \boldsymbol{E}_e(t)dt. \tag{26}$$

In Eq. (26), T denotes the period associated with the center frequency of excitation. The average total energy over the last 20 time intervals (1 period) is depicted in Fig. 12c, where the colorbar indicates Joules (J). The maximum displayed energy level has been limited to 2.3 mJ to allow the illustration of caustics immediately preceding the appearance of reflected waves from the boundaries. At the location of the applied load, the maximum energy for the considered time interval is 1.3 J. The energy flux resulting from a point load with $\Omega = 1.62$ follows the preferential directions or caustics indicated by the corresponding group velocities. In nonlinear, hyperbolic, partial-differential equations such convergence of rays (directions normal to the wave-front) leads to high amplitude waves, which in turn tend to accelerate and thus avoid singularities [32]. For the case at hand, the strain in the ligaments and nodes of the lattice within the caustic region and outside it is reported in Fig. 12c. The strain reported in Fig. 12c appears finite and small ($\approx 1\ \mu\varepsilon$) within the time of integration of seven wave periods. This may suggest that the nature of this focusing phenomenon may not be nonlinear with respect to deformations; at least in short-time evolution. In solids furthermore, elastic wave caustics, or at least the caustic phenomena reported here and in [29–31], may be attributed to anisotropy and are explained in terms of Christoffel equations [18,20]. This approach is based on the knowledge of elastic constants and neglects nonlinear deformations. In the current work, the equivalent homogeneous elastic constants are not known, negating an analytical investigation of pertinent wave equations. Future work is certainly needed to better assess the nature of this phenomenon.

The energy focusing suggested by caustics and present in all considered wave modes, nonetheless, notably features a complex dependency upon frequency ω; the orientation and extent of cusps in the group velocity diagrams, in fact, change according to both wave modes and frequencies. Chiral lattices, hence, offer the flexibility to steer elastic waves along desired directions. This could be accomplished by simply changing the excitation frequency of a disturbance-producing source.

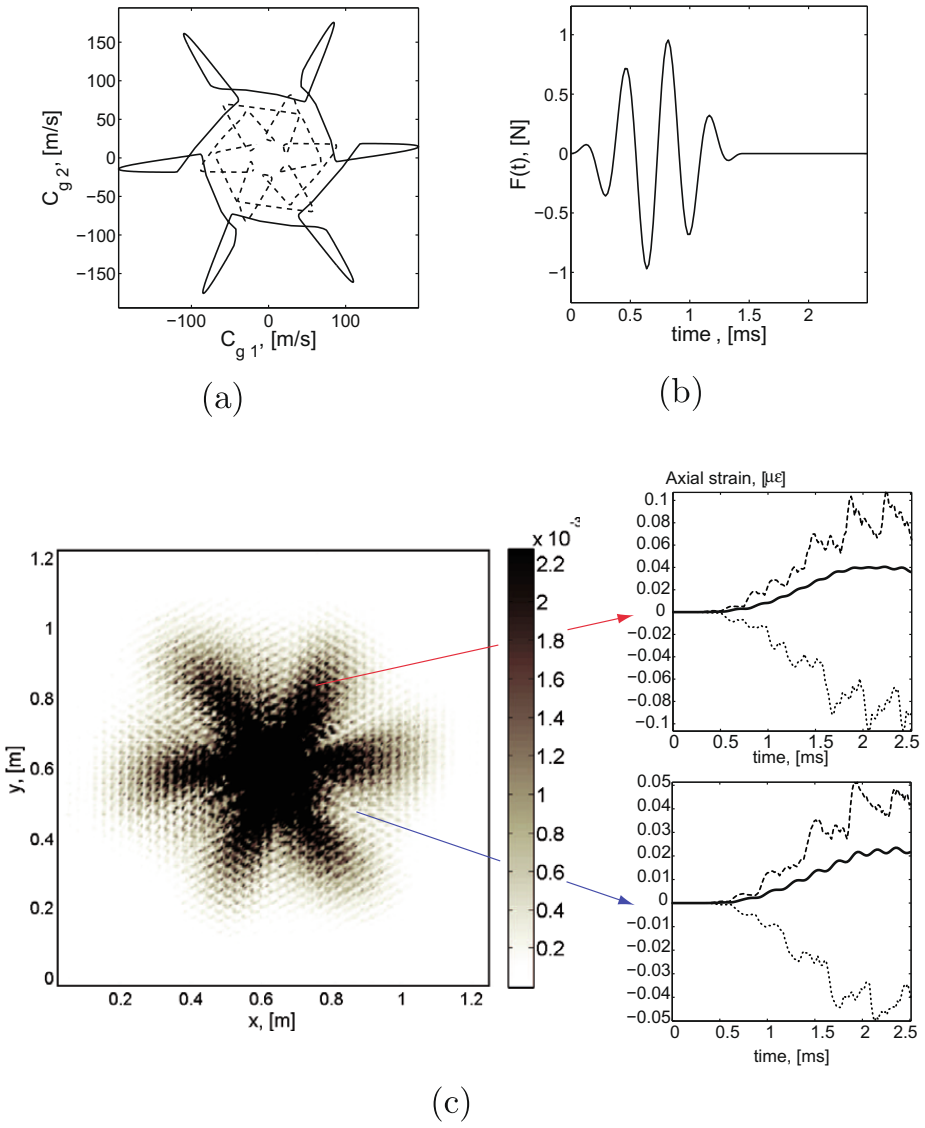

Fig. 12. Group velocity corresponding to first and second wavemodes (– mode 1, – mode 2) and $\Omega = 1.62$ (a), applied load history (b) and corresponding average energy (J) with rms strain (black line), upper (dashed line) and lower bounds (dotted line) in microstrain units [$\mu\varepsilon$] inside and outside the caustic region (c).

5. Summary

In-plane wave propagation in chiral lattices is investigated through the application of Bloch analysis. The considered lattice features in-plane hexagonal geometry as well as chirality, and it is characterized by a set of parameters which significantly affect its elasto-dynamic behavior. The occurrence of band gaps, anisotropic behavior, and the dispersive characteristics of the considered lattices are evaluated for various combinations of characteristic geometric parameters. Of particular relevance are unique features such as strongly anisotropic behavior at higher frequencies, the significant dependence of band gap widths and center frequency on a limited set of characteristic geometric parameters, and the occurrence of caustics. The presented results suggest the possibility of utilizing the considered class of lattices for the design of novel phononic meta-materials.

References

[1] K.E. Evans, Design of doubly curved sandwich panels with honeycomb cores, Comp. Struct. 17 (2) (1991) 95–111.
[2] F. Scarpa, G. Tomlinson, Theoretical characteristics of the vibration of sandwich plates with in-plane negative poissons ratio values, J. Sound Vibrations 230 (1) (2000) 45–67.
[3] M. Ruzzene, F. Scarpa, F. Soranna, Wave beaming effects in two-dimensional cellular structures, Smart Mater. Struct. 12 (3) (2003) 363–372.
[4] A.S. Phani, J. Woodhouse, N.A. Fleck, Wave propagation in two-dimensional periodic lattices, J. Acoust. Soc. Am. 119 (4) (2006) 1995–2005.
[5] I.E. Psarobas, Phononic crystals, sonic band-gap materials, J. Struct., Phys., Chem. Aspects Cryst. Mater. 220 (2003) 9–10.
[6] M.I. Hussein, G. Hulbert, R. Scott, Tailoring of wave propagation characteristics in periodic structures with multilayer unit cells, in: Proceedings of 17th American Society of Composites Technical Conference, 2002.

[7] M.I. Hussein, K. Hamza, G. Hulbert, K. Saitou, Optimal synthesis of 2d phononic crystals for broadband frequency isolation, Waves Random Complex Media 17 (4) (2007) 491–510.
[8] O. Sigmund, J. Jensen, Systematic design of phononic band-gap materials and structures by topology optimization, Phylosophical Trans. Roy. Soc. London, Series A, Math. Phys. Eng. Sci. 361 (1806) (2003) 1001–1019.
[9] A. Diaz, A. Haddow, L. Ma, Design of band-gap grid structures, Struct. Multidisciplinary Optimization 29 (6) (2005) 418–431.
[10] D. Prall, R.S. Lakes, Properties of a chiral honeycomb with a poisson's ratio −1, Int. J. Mech. Sci. 39 (1996) 305–314.
[11] K. Wojciechowski, Two-dimensional isotropic system with a negative poisson ratio, Phys. Lett. A 137 (1989) 60–64.
[12] A. Spadoni, M. Ruzzene, F. Scarpa, Dynamic response of chiral truss-core assemblies, J. Intelligent Mater. Syst. Struct. 17 (11) (2005) 941–952.
[13] A. Spadoni, M. Ruzzene, Static aeroelastic response of chiral-core airfoils, J. Intelligent Mater. Syst. Struct. 18 (2007) 1067–1075.
[14] R.D. Cook, D.S. Malkus, M.E. Plesha, R.J. Witt, Concepts and Applications of Finite Element Analysis, fourth ed., Wiley, 2001.
[15] B.D. Agarwal, L.J. Broutman, Analysis and Performance of Fiber Composites, John Wiley, New York, 1980.
[16] A.E.H. Love, A Treatise on the Mathematical Theory of Elasticity, 4th ed., Dover Publications, 1927 (Chapter VI, Section 110).
[17] L. Brillouin, Wave Propagation in Periodic Structures, Dover, New York, NY, 1953.
[18] B.A. Auld, Acoustic Fields and Waves in Solids, second ed., Vol. 1, Krieger Publ. Co., Malabar, FL, 1990.
[19] K.-J. Bathe, Finite Element Procedures, 1st ed., Prentice Hall, Upper Saddle River, NJ, 1996.
[20] J.P. Wolfe, Imaging Phonons: Acoustic Wave Propagation in Solids, Cambridge University Press, 1998.
[21] S. Gonella, M. Ruzzene, Homogenization and equivalent in-plane properties of two-dimensional periodic lattices, Int. J. Solids Struct. 45 (10) (2008) 2897–2915.
[22] R.S. Lakes, Elastic and viscoelastic behavior of chiral materials, Int. J. Mech. Sci. 43 (7) (2001) 1579–1589.
[23] J.N. Grima, R. Gatt, P.-S. Farrugia, On the properties of auxetic meta-tetrachiral structures, Phys. Status Solidi B 245 (2008) 511–520.
[24] I.G. Masters, K.E. Evans, Models for the elastic deformation of honeycombs, Compos. Struct. 35 (4) (1996) 403–422.
[25] D. Bornengo, F. Scarpa, C. Remillant, Morphing airfoil concept with chiral core structure, I MECH E Part G, J. Aerospace Eng. G3 (8) (2005) 185–192.
[26] C. Pierre, Mode localization and eigenvalue loci veering phenomena in disordered structures, Develop. Mech. 14 (1987) 165–170.
[27] H. Chan, J. Liu, Mode localization and frequency loci veering in disordered engineering structures, Chaos, Solitons Fractals 11 (10) (2000) 1493–1504.
[28] N. Perkins, C. Mote, Comments on curve veering in eigenvalue problems, J. Sound Vibration 106 (3) (1986) 451–463.
[29] B. Taylor, H.J. Maris, C. Elbaum, Phonon focusing in solids, Phys. Rev. Lett. 23 (1969) 416.
[30] B. Taylor, H.J. Maris, C. Elbaum, Focusing of phonons in crystalline solids due to elastic anisotropy, Phys. Rev. B 3 (1971) 1462.
[31] H.J. Maris, Enhancement of heat pulses in crystals due to elastic anisotropy, J. Acoustical Soc. Am. 50 (1971) 812.
[32] G.B. Whitham, Linear and Nonlinear Waves, Wiley Interscience, New York, NY, 1999.